

## AN EXAMINATION OF THE X-RAY SOURCES IN THE GLOBULAR CLUSTER NGC 6652

W. S. STACEY<sup>1</sup>, C. O. HEINKE<sup>1,2</sup>, H. N. COHN<sup>3</sup>, P. M. LUGGER<sup>3</sup>, A. BAHRAMIAN<sup>1</sup>

*Draft version November 13, 2018*

### ABSTRACT

We observed the globular cluster NGC 6652 with *Chandra* for 47.5 ks, detecting six known X-ray sources, as well as five previously undetected X-ray sources. Source A (XB 1832-330) is a well-known bright low-mass X-ray binary (LMXB). The second brightest source, B, has a spectrum that fits well to either a power-law model ( $\Gamma \sim 1.3$ ) or an absorbed hot gas emission model ( $kT \sim 34$  keV). Its unabsorbed 0.5-10 keV luminosity ( $L_X = 1.6^{+0.1}_{-0.1} \times 10^{34}$  erg s<sup>-1</sup>) is suggestive of a neutron star primary; however, Source B exhibits unusual variability for a LMXB, varying by over an order of magnitude on timescales of  $\sim 100$  s. Source C's spectrum contains a strong low-energy component below  $\sim 1$  keV. Its spectrum is well fit to a simplified magnetic cataclysmic variable (CV) model, thus the soft component may be explained by a hot polar cap of a magnetic CV. Source D has an average  $L_X$  (0.5-10 keV)  $\sim 9 \times 10^{32}$  erg s<sup>-1</sup> and its spectrum is well fit to a neutron star atmosphere model. This is indicative of a quiescent neutron star LMXB, suggesting Source D may be the third known LMXB in NGC 6652. Source E has  $L_X$  (0.5-10 keV)  $\sim 3 \times 10^{32}$  erg s<sup>-1</sup>, while Source F has  $L_X$  (0.5-10 keV)  $\sim 1 \times 10^{32}$  erg s<sup>-1</sup>. Their relatively hard X-ray spectra are well-fit by power-law or plasma emission models. Five newly detected fainter sources have luminosities between  $1-5 \times 10^{31}$  erg s<sup>-1</sup>. NGC 6652 has an unusually flat X-ray luminosity function compared to other globular clusters, which may be connected to its extremely high central density.

*Subject headings:* binaries : X-rays — cataclysmic variables — globular clusters: individual (NGC 6652) — stars: neutron

### 1. INTRODUCTION

Low-luminosity X-ray sources in globular clusters were identified with Einstein (Hertz & Grindlay 1983) as a separate class of X-ray sources from bright ( $10^{36} < L_X < 10^{38}$  ergs/s) LMXBs containing neutron stars (NSs). They suggested that low-luminosity sources were primarily cataclysmic variables (CVs), with similar accretion rates to the LMXBs but potential energy wells 1000 times shallower, but also including some NS LMXBs in quiescence (qLMXBs). Verbunt et al. (1984) argued that the brightest low- $L_X$  systems ( $L_X > 10^{33}$  ergs/s) were too bright to be CVs, and must be qLMXBs. The answer, from *Chandra* observations, has been mixed; some of the brighter low- $L_X$  systems have been identified with qLMXBs, and some with CVs (e.g. in 47 Tuc, Grindlay et al. 2001a).

The brighter low- $L_X$  systems ( $5 \times 10^{32} < L_X < 10^{35}$  ergs/s) are of special interest. The bright CVs in this range are at the top of the X-ray luminosity distribution of CVs. As disk-fed CVs transition to optically thick flows at high mass transfer rates, suppressing hard X-rays (Patterson & Raymond 1985), it is thought that reaching high X-ray luminosities may require magnetically channeled accretion (permitting optically thin flows) onto massive white dwarfs (e.g. Grindlay et al. 1995; Ivanova et al. 2006). The relative lack of dwarf novae outbursts in globular clusters also supports the magnetically channeled accretion idea (Shara et al. 1996).

However, there is little *direct* evidence for magnetic CVs in globular clusters; published evidence consists of  $\lambda 4686$  He II emission (associated with intermediate polar CVs, in which the accretion disk is truncated by the primary's B field) from 3 CVs in NGC 6397 (Edmonds et al. 1999), and very soft blackbody-like components in the CVs X10 in 47 Tuc (Heinke et al. 2005) and 1E 1339.8+2837 in M3 (Stacey et al. 2011). Further evidence of the nature of the most luminous CVs, in particular direct evidence of strong magnetic fields, will be important.

The most luminous qLMXBs ( $10^{35} > L_X > 10^{34}$  ergs/s) are brighter than the expected emission from residual heat in the crust (Yakovlev & Pethick 2004), so must be powered by continuing accretion. However, they are fainter than expected for X-ray binaries undergoing outbursts driven by the standard disk instability model (e.g. King 2000; Wijnands et al. 2006). We don't yet understand the behavior of LMXBs that maintain these intermediate luminosities for years, such as XMMU J174716.1–281048 (Del Santo et al. 2007) and M15 X-3 (Heinke et al. 2009). The neutron star's magnetic field is expected to exercise a “propeller effect” which should stop the accretion of material onto the neutron star surface at low mass transfer rates (Illarionov & Sunyaev 1975). On the other hand, simulations of the interaction of weak accretion with a magnetic propeller predict some material will reach the neutron star (e.g. Romanova et al. 2002), suggesting that NS LMXBs in a propeller state might produce accretion at intermediate luminosities.

NGC 6652 contains a moderately bright ( $L_X = 10^{36}$  ergs/s) LMXB (A). Three other sources were identified in a 1.6 ksec *Chandra* HRC observation in 2001 (Heinke et al. 2001). The brightest faint source, B, at  $L_X(0.5-7) \sim 6 \times 10^{33}$  ergs/s, has an optically (Hubble

<sup>1</sup> University of Alberta Physics Dept., CCIS 4-183, Edmonton, AB T6G 2E1, Canada

<sup>2</sup> Ingenuity New Faculty; heinke@ualberta.ca

<sup>3</sup> Department of Astronomy, Indiana University, 727 East 3rd St., Bloomington, IN 47405, USA

Space Telescope, HST) identified blue variable counterpart (Deutsch et al. 1998). It is UV-bright but appears on the main sequence in a  $V$  vs.  $V - I$  color-magnitude diagram, suggesting a quiescent LMXB with a weak disk (Heinke et al. 2001). A 5-ks 2008 *Chandra* observation showed rapid variability, from  $2 \times 10^{33}$  up to  $> 5 \times 10^{34}$  ergs/s on timescales  $< 2$  minutes, not previously seen from LMXBs at such low luminosities. Spectral fitting of countrate-selected bins suggested spectral variability, but it was unclear whether the behavior was true flaring or variations in obscuring column from an edge-on source (Coomber et al. 2011).

The next brightest source, C, is very blue in  $V - I$  HST observations, which combined with its  $L_X$  of  $6 \times 10^{32}$  ergs/s, indicates it is likely a very luminous CV (Heinke et al. 2001). The 5-ks *Chandra* observation found an extremely soft spectrum, with most of the 90 counts below 0.8 keV (Coomber et al. 2011). D, at  $L_X = 5 \times 10^{32}$  ergs/s in the (optically crowded) cluster core, also showed a soft spectrum, with a suggestion of a line in the (73-count) spectrum. The 5-ks *Chandra* observation revealed three other faint sources, of which G lies outside our field of view.

NGC 6652 has been considered to be a cluster of only moderate central density (Harris 2010) and stellar encounter rate (Verbunt 2003), making its possession of a bright LMXB somewhat unusual. However, a recent surface brightness profile from Noyola & Gebhardt (2006) finds a sharp core with a significantly higher central surface brightness than previously measured, identifying it as a core-collapsed cluster. We have computed the central luminosity densities of Galactic globular clusters using the Noyola & Gebhardt parameter updates, and note that NGC 6652's central density is the fifth highest.

## 2. DATA REDUCTION

We observed the globular cluster NGC 6652 on June 3rd, 2011 with the *Chandra* ACIS-S detector, using two active CCDs (S2 and S3) with a 1/8 subarray to abate pileup from Source B. The total observation time was 47.5 ks. The data were reduced using CIAO version 4.3<sup>4</sup>. A new bad pixel file was generated with the CIAO *acis\_run\_hotpix* tool. The observations were further processed using *acis\_process\_events* and filtered<sup>5</sup> in order to create level 2 event files, as detailed in the CIAO Science Threads<sup>6</sup>.

We ran the CIAO *wavdetect* tool<sup>7</sup> over an energy range of 0.5–10 keV. From this, we found six X-ray sources, all located within the cluster half-mass radius (Figure 1). A seventh previously detected source (Coomber et al. 2011) lay outside our field of view. The source positions agree with our previous 2008 *Chandra* observation. In addition, we ran *wavdetect* over several other ranges (0.3–7 keV, 0.3–2 keV, 2–7 keV); however, no previously undetected sources were found. We further ran *PWDetect*<sup>8</sup> (Damiani et al. 1997a,b) over a range of 0.3–7 keV. Both *PWDetect* and *wavdetect* use wavelet transforms to locate possible sources; we have found that *wavdetect* ef-

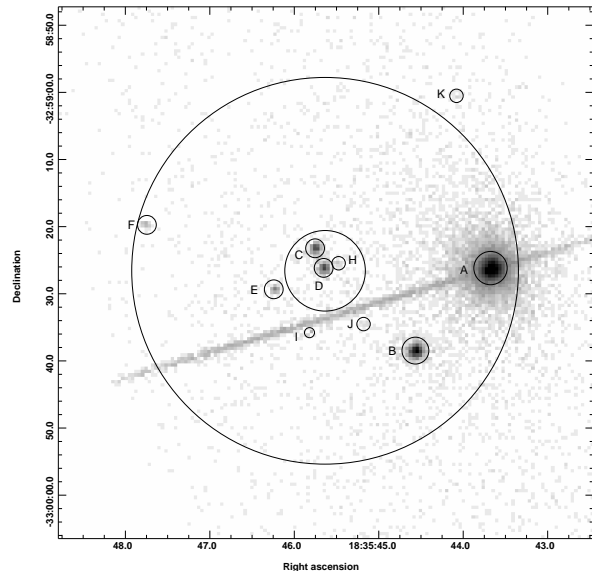


FIG. 1.— ACIS-S image of NGC 6652 over 0.3–7 keV, with X-ray sources are labeled. The core radius ( $0.10'$ ) and half-mass radius ( $0.48'$ ) are shown (Harris 2010). A previously detected X-ray source (Source G) lies outside our field of view (see Coomber et al. (2011)), while Source L lies  $\sim 1.4'$  from the center of the cluster.

ficiently finds sources without spurious detections over large uncrowded fields of view, while *PWDetect* can more effectively identify faint sources near bright sources, though it has a higher spurious detection rate, making it less suitable for large fields (e.g. Heinke et al. 2003a; Bogdanov et al. 2010). In order to reduce the number of spurious detections, we only include detections above  $5\sigma$ . We identify four previously undetected X-ray sources within the cluster half-mass radius (Sources H through K) and one source outside the cluster half-mass radius (Source L). Our detection limit of 10 counts translates to roughly  $1 \times 10^{31}$  ergs/s (0.5–2.5 keV), or  $2 \times 10^{31}$  ergs/s (0.5–10 keV) for standard absorbed powerlaw spectra with photon index=2 at the 10 kpc cluster distance (Harris 2010).

We selected events within a circle around the sources (radius  $1''$  for H, J, K and L, radius  $0.75''$  for I, due to its proximity to the readout streak), and background from local regions, determining the background subtracted source counts. The positions and net counts for each observed source are listed in Table 1, with 95% confidence positional uncertainty values from equation (5) of Hong et al. (2005). For Sources B through F, we selected events from a circular source region ( $2''$  for B,  $1.4''$  for C through F) centered on the *wavdetect* positions. For Sources B, E and F, an annulus of inner radius  $5''$  that excluded the source was chosen for the background. Due to the proximity of Sources C and D, a larger annulus of inner radius  $6''$  that excluded both sources was chosen for the background. Using these regions, the CIAO *specextract* script was run to extract source and background spectra, generating RMF and ARF files. XSPEC version 12.7<sup>9</sup> was used to examine and fit the spectra

<sup>4</sup> <http://cxc.cfa.harvard.edu/ciao/>

<sup>5</sup> <http://cxc.cfa.harvard.edu/ciao/threads/createL2/>

<sup>6</sup> <http://cxc.cfa.harvard.edu/ciao/threads/all.html>

<sup>7</sup> <http://cxc.harvard.edu/ciao/threads/wavdetect/>

<sup>8</sup> [http://www.astropa.unipa.it/progetti\\_ricerca/PWDetect/](http://www.astropa.unipa.it/progetti_ricerca/PWDetect/)

<sup>9</sup> <http://heasarc.gsfc.nasa.gov/docs/xanadu/xspec/>

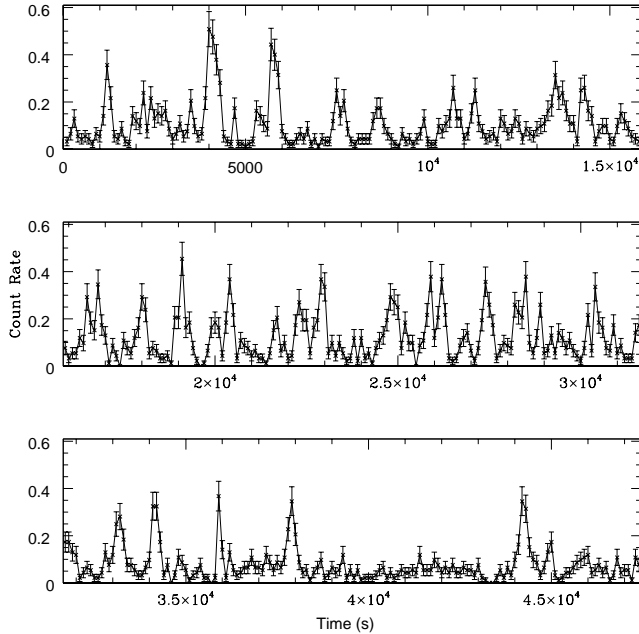


FIG. 2.— ACIS lightcurve extracted from Source B in the energy band 0.3–7 keV, using a binning of 100 s. The lightcurve is split into three consecutive periods (top, middle and bottom) in order to clearly display the peaks in the lightcurve. A corresponding variability index of 10 (variable) was found using the CIAO *glvary* tool (discussed in the following sections).

### 3. X-RAY ANALYSIS

#### 3.1. Source A

We extracted 1537 counts from Source A’s readout streak (using a 99.5 by 3.5 pixel box region), grouping them into 14 bins with a minimum of 100 counts per bin. We were able to successfully ( $\chi^2_\nu=1.05$  for 11 degrees of freedom) fit Source A’s spectrum to an absorbed power-law model ( $\Gamma = 1.9 \pm 0.3$ ), with  $L_X(0.5\text{--}10\text{ keV})=7.0^{+0.7}_{-0.7} \times 10^{35}$  ergs/s. A hydrogen column density of  $27^{+11}_{-9} \times 10^{20}\text{ cm}^{-2}$  was measured, significantly larger than the cluster value of  $5 \times 10^{20}\text{ cm}^{-2}$  (Harris 2010). Previous studies of A’s X-ray spectrum with ASCA, BeppoSAX, and XMM (Mukai & Smale 2000; Parmar et al. 2001; Sidoli et al. 2008) agree in requiring additional intrinsic absorption, with their single-component best-fit spectra resembling ours. Those previous observations (optimized for this bright source) were able to better constrain A’s spectrum, measuring partial covering and multiple spectral components, which our data are insufficient to constrain.

#### 3.2. Source B

##### 3.2.1. Timing Analysis

A 474 bin lightcurve (100 s/bin) was extracted for Source B using the CIAO *dmextract* tool (Fig. 2). The observation shows clear variability by factors over an order of magnitude on timescales of  $\sim 100$  s, uncharacteristic of low-mass X-ray binaries. We verified the variability with the CIAO *glvary* tool, which applies the Gregory-Loredo algorithm. The algorithm separates the observation into bins based upon time and

looks for significant variation, returning a variability index (Gregory & Loredo 1992). For Source B, a variability index of 10 was found, corresponding to a variability probability of  $\sim 1.0$ . Power spectra (generated using XRONOS<sup>10</sup>) show no clear periodicity in Source B’s X-ray emission (using either 100 s or 0.54 s binning). In order to test whether the variation may be due to changes in the obscuring column, the observation was filtered into eight separate ranges based upon the count rate. The count rate ranges were chosen to ensure each range contains at least 400 counts. The hardness ratio within each range was then quantified by examining the ratio of the number of counts with photon energy between 0.3–1 keV to the number of counts with photon energy between 0.3–7 keV (see Table 2). If the variation was due to obscuration, we would expect to find the lowest hardness ratios in the lowest count rate range. This is seen to some degree as the lowest hardness ratio ( $0.16 \pm 0.02$ ) is found between 0.05–0.1 counts  $\text{s}^{-1}$  and the largest hardness ratio ( $0.23 \pm 0.02$ ) is seen between 0.27–0.35 counts  $\text{s}^{-1}$ . We further examined the spectrum for each of these ranges (below).

##### 3.2.2. X-ray Spectral Analysis

Source B’s total spectrum was binned (using the GRPPHA tool) so that each bin contained a minimum of 100 counts. We included a photoelectric absorption component (XSPEC model *phabs*) with each model, leaving the hydrogen column density,  $N_H$ , as a free parameter. The metal abundance for the *mekal* model was kept at  $[\text{Fe}/\text{H}] = -0.81$  (Harris 1996)<sup>11</sup>. Considering a range from 0.5 to 10 keV, Source B’s spectrum was fit reasonably well to both an absorbed power-law model (XSPEC model *pegpwrhw*, photon index  $\Gamma = 1.3 \pm 0.1$ ) and an absorbed hot X-ray plasma model (XSPEC model *mekal*, temperature  $kT=34^{+28}_{-13}$  keV). We found an unabsorbed X-ray flux (0.5–10 keV) of  $(1.4 \pm 0.1) \times 10^{-12}$  erg  $\text{cm}^{-2}\text{ s}^{-1}$  from the power-law model and  $(1.3 \pm 0.1) \times 10^{-12}$  erg  $\text{cm}^{-2}\text{ s}^{-1}$  from the plasma emission model. Using a distance of 10.0 kpc (Harris 1996), these correspond to luminosities of  $(1.7 \pm 0.1) \times 10^{34}$  erg  $\text{s}^{-1}$  and  $(1.6 \pm 0.1) \times 10^{34}$  erg  $\text{s}^{-1}$ , consistent with the 2008 *Chandra* ACIS-S observation. The full results are listed in Table 3.

We next filtered the spectrum into eight separate ranges based upon count rate in order to look for possible changes in the spectra. Using a minimum of 30 counts per bin, we fit the spectra to an absorbed *mekal* model over 0.5 to 10 keV (Figure 3). In addition, the five spectra with the largest count rates contained a pileup component (grade morphing parameter fixed at 0.5, Davis 2001). The X-ray plasma emission temperature and normalization, as well as the hydrogen column density ( $N_H$ ), were allowed to vary. The parameters from these fits are listed in Table 2. There appears to be a tendency for the higher count rate spectra to have lower  $N_H$  values, as the highest  $N_H$  observed appears in the 0.05–0.075 counts  $\text{s}^{-1}$  range and the lowest appears in the 0.27–0.35 counts  $\text{s}^{-1}$  range. However, this tendency is not strong; the maximum fitted  $N_H$  is only  $2.7^{+1.5}_{-1.4} \times 10^{21}\text{ cm}^{-2}$ , insufficient to significantly decrease the countrate. Therefore, we rule

<sup>10</sup> <http://heasarc.nasa.gov/xanadu/xronos/xronos.html>

<sup>11</sup> Updated 2010; <http://www.physics.mcmaster.ca/~harris/mwgc.dat>

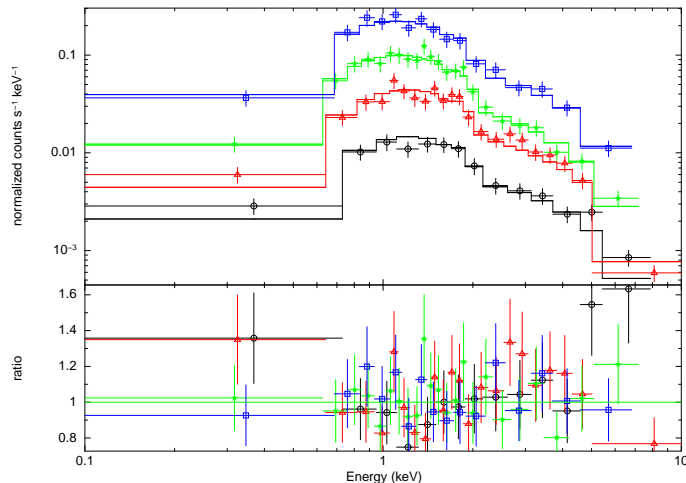


FIG. 3.— X-ray spectra of Source B, with a minimum of 30 counts per bin. Spectra are filtered by count rate ranges, with best-fit absorbed *mekal* models fit from 0.5 to 10 keV. Eight separate ranges were fit to produce the results in Table 2 but for clarity only four are shown here. From highest to lowest count rate, these are  $>0.35$  counts  $s^{-1}$  (blue, squares),  $0.15 - 0.2$  counts  $s^{-1}$  (green, stars),  $0.075 - 0.1$  counts  $s^{-1}$  (red, triangles) and  $<0.05$  counts  $s^{-1}$  (black, circles). The ratio of the data to the model is shown below.

out that the flux variations are entirely due to obscuration by changing  $N_H$  columns, e.g. due to an edge-on accretion disk.

We placed Source B (as well as the other observed sources) on an X-ray color-magnitude diagram (Figure 4). We defined color to be  $2.5 \log[(0.5-1.5 \text{ keV counts})/(1.5-7.0 \text{ keV counts})]$  and plotted it against the 0.5–10 keV luminosity of the sources. In addition, we plotted the X-ray color predictions for power-law and *mekal* models, as well as the X-ray color-luminosity relation for the *nsatmos* model.

### 3.3. Source C

A lightcurve (500 s/bin) was extracted for Source C (see Figure 5). Using the CIAO *glvary* tool (discussed in Section 3.2.1) a variability index of 7 was found, with a corresponding variability probability of 0.995. Power spectra show no clear evidence of periodicity. The total unabsorbed luminosity from the simplified polar CV model (below) is  $L_X$  (0.5–10 keV) =  $1.6^{+0.7}_{-0.2} \times 10^{33}$  erg  $s^{-1}$ , which is comparable to the 2008 ACIS-S observation which found  $L_X$  (0.5–10 keV) =  $1.2^{+0.1}_{-0.5} \times 10^{33}$  erg  $s^{-1}$  (Coomber et al. 2011).

Grouping Source C’s spectrum into bins with a minimum of 30 counts each, a notable low energy component below  $\sim 1$  keV was found (Figure 6). At energies below  $\sim 0.5$  keV, the accuracy of the *Chandra* response files and the sensitivity of the ACIS-S detector are no longer optimal. For this reason, we only considered a range from 0.5 to 10 keV for our primary fits. Even so, we were unable to adequately model Source C to any single component model (see Table 3). Allowing the  $N_H$  to vary, we successfully fit the spectrum to a model containing two hot X-ray plasma emission components (XSPEC model *mekal*) with temperatures  $>17$  keV and  $0.18 \pm 0.03$  keV. Double *mekal* models are commonly used to describe the spectra of CVs (Baskill et al. 2005); however, Source C’s lower-energy component is unusually strong. In order to examine the lower energy emission, we fit the same

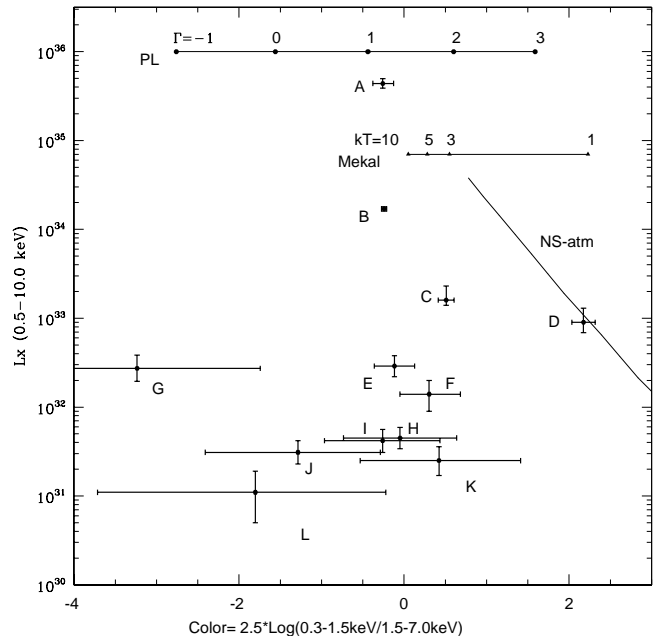


FIG. 4.— X-ray color-magnitude diagram for detected sources. Color is determined as a function of low-energy to high energy counts. X-ray luminosity (0.5–10 keV) is plotted along the vertical axis. Errors are derived for  $1 \sigma$  from Gehrels (1986). Values for Sources A and G are taken from Coomber et al. (2011). Additionally, the theoretical colors for absorbed power-law, *mekal* and *nsatmos* models (with the corresponding  $L_X$  for *nsatmos*) are shown.

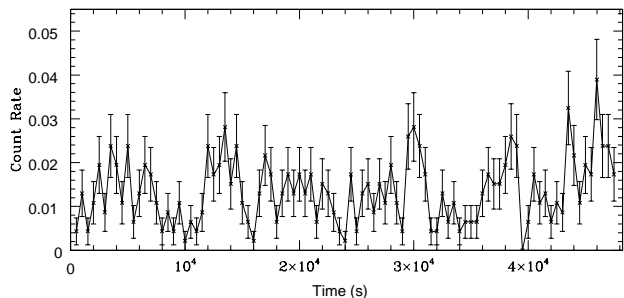


FIG. 5.— ACIS lightcurve extracted from Source C over 0.3–7 keV, using a binning of 500 s. The CIAO *glvary* tool gave a variability index of 7 (variable).

double *mekal* model over 0.2 to 10 keV; however, this failed to produce an acceptable fit ( $\chi^2_\nu = 1.99$ ). Source C’s spectrum was adequately fit to a simplified polar CV model, containing a high-temperature *mekal* component and a soft blackbody component (e.g. Ramsay et al. 2004). Again, allowing the  $N_H$  to vary, the best fit model resulted in a *mekal* temperature  $>18$  keV and a blackbody temperature of  $70 \pm 20$  eV. Fitting down to 0.2 keV with this model gave a better fit than the double *mekal* model in the same range ( $\chi^2_\nu = 0.95$ , *mekal* temperature  $> 14$  keV, blackbody temperature of  $80 \pm 10$  eV).

### 3.4. Source D

The lightcurve from Source D showed no evidence of variation. A variability index (discussed in Section 3.2.1) of 0 was found, resulting in a low variability probability of 0.033.

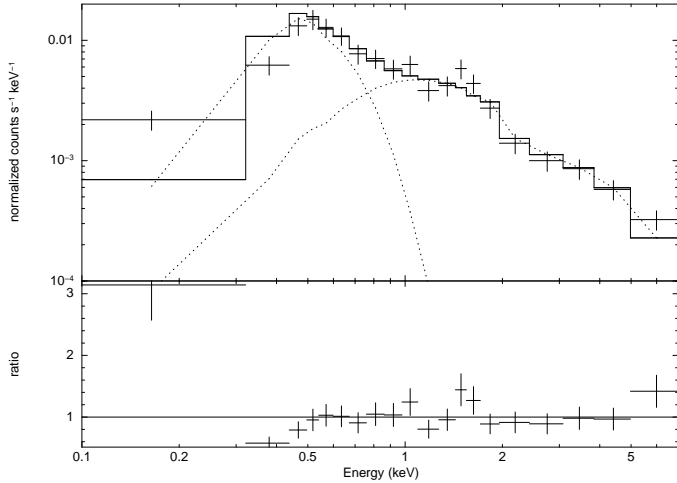


FIG. 6.— *Chandra* spectrum of Source C fit to an absorbed *mekal* plus blackbody model from 0.5 to 10 keV, with a minimum of 30 counts per bin. The dotted lines indicate the two components of the model (*mekal* being of higher energy). The ratio of the data to the model is shown below. Resulting parameters from the fit are listed in Table 3.

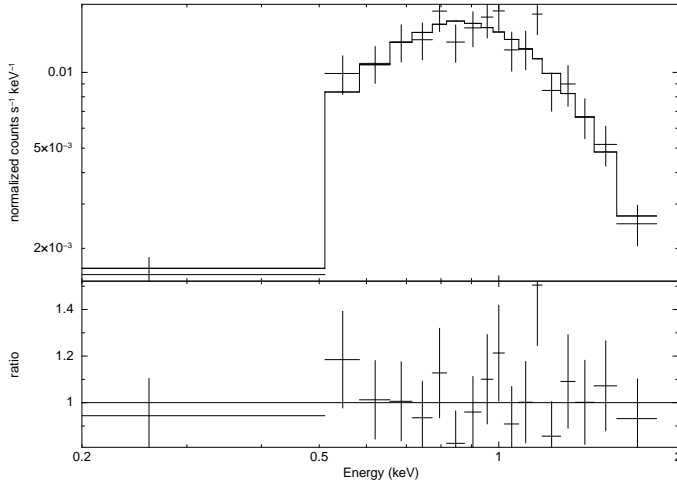


FIG. 7.— *Chandra* spectrum of Source D fit to an absorbed neutron star atmosphere model from 0.5 to 10 keV, with a minimum of 30 counts per bin. The ratio of the data to the model is shown below. Resulting parameters from the fit are listed in Table 3.

Source D’s spectrum was extracted and grouped to ensure a minimum of 30 counts per bin (Figure 7). Including a photon absorption component and allowing the  $N_H$  to vary, Source D was fit to a power-law model resulting in a photon index of  $5.8^{+0.8}_{-1.2}$  (see Table 3). The fitted  $N_H$  of  $(42^{+14}_{-19}) \times 10^{20} \text{ cm}^{-2}$  is much larger than the cluster value of  $5 \times 10^{20} \text{ cm}^{-2}$ , and the high power-law photon index suggests testing thermal emission models. A *mekal* model proved to be a poor fit; however, a neutron star atmosphere model (XSPEC model *nsatmos*,  $1.4 M_\odot$ , radius of 10 km) proved to sufficiently fit the spectrum. From this we found an effective temperature of  $111 \pm 2 \text{ eV}$ . We used the XSPEC *cflux* model to find  $L_X$  (0.5–10 keV) =  $9.0^{+4.0}_{-2.1} \times 10^{32} \text{ erg s}^{-1}$ , consistent with the 2000 *Chandra* HRC observation and the 2008 *Chandra* ACIS observation. Our previous *Chandra* observation (Coomber et al. 2011) suggested the existence of an emission line near 1 keV; however, our higher-quality spectrum shows no evidence for this.

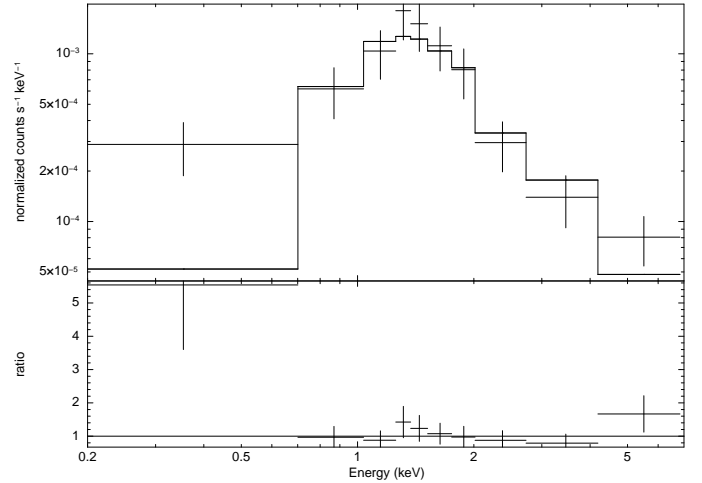


FIG. 8.— *Chandra* spectrum of Source E fit to an absorbed power-law model over 0.5 to 10 keV, with a minimum of 10 counts per bin. The ratio of the data to the model is shown below. Resulting parameters from the fit are listed in Table 3.

### 3.5. Sources E + F

We detected 99 counts from Source E and 35 counts from Source F. The relatively low number of counts reduces the accuracy of timing analysis; however, it is still possible to use the CIAO *glvary* tool to look for strong variation. A variability probability of 0.78 was found for Source E (variability index of 2) and a variability probability of 0.45 was found for Source F (variability index of 0), thus we do not have strong evidence of variability in either.

The spectrum for Source E was extracted and grouped to ensure a minimum of 10 counts per bin (see Figure 8). To ensure optimal accuracy from the *Chandra* response files, we considered an energy range from 0.5 to 10 keV. Allowing the  $N_H$  to vary, Source E was successfully fit to both an absorbed power-law model with photon index of  $2.2^{+1.1}_{-0.8}$  and an absorbed *mekal* model with temperature  $> 1.8 \text{ keV}$  (Table 3). An unabsorbed 0.5–10 keV luminosity of  $2.9^{+0.9}_{-0.7} \times 10^{32} \text{ erg s}^{-1}$  was determined from the *mekal* model, consistent with our previous 2008 *Chandra* observation.

The spectrum for Source F was also grouped to ensure a minimum of 10 counts per bin, resulting in a total of four bins (Figure 9). Due to the low number of bins, the entire 0–10 keV range was considered. We were unable to find an ideal single-component model with which to fit Source F. An absorbed *nsatmos* model proved a poor fit, while the null hypothesis probability (NHP) for both an absorbed power-law ( $\Gamma = 1.7^{+1.1}_{-0.5}$ , NHP = 0.31) and an absorbed *mekal* model (temperature  $> 1.9 \text{ keV}$ , NHP = 0.29) remained high. Using the C-statistic (Cash 1979), we further examined the suitability of each model by fitting the unbinned data. For the power-law model 99.9% of simulated spectra resulted in lower C-statistic values, while 99.7% did for the *mekal* model and 100% did for the *nsatmos* model (for  $10^4$  simulated spectra), suggesting a poor fit in each case. The power-law and *mekal* parameters for the unbinned fitting agree within error to the binned fitting parameters ( $\Gamma < 6.0$ ,  $kT = 1.8^{+2.8}_{-0.5}$ ). The unbinned *nsatmos* model results in a marginally lower temperature of  $85^{+10}_{-8} \text{ eV}$ . The luminosity obtained for

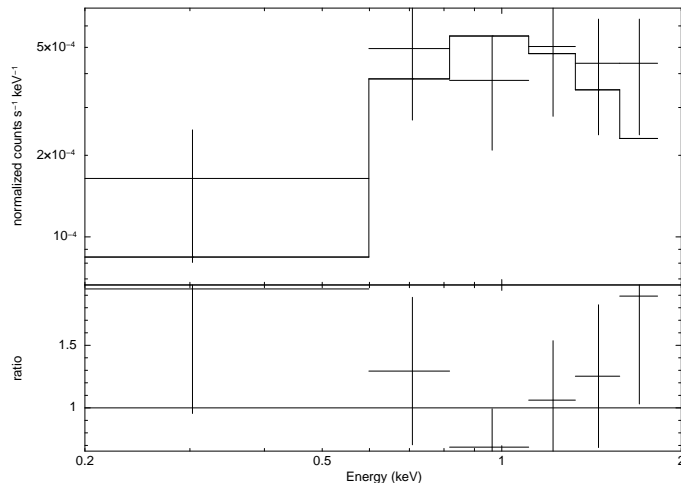


FIG. 9.— *Chandra* spectrum of Source F. The model was determined using the C-statistic, fitting an absorbed *mekal* model to the unbinned data over 0 to 10 keV. For clarity only, the spectrum is shown with a minimum of 5 counts per bin. The ratio of the data to the model is shown below. Resulting parameters from the fit are listed in Table 3.

Source F (Table 3) was consistent with the previous 2008 *Chandra* observation.

### 3.6. Faint Sources

The five faintest sources have too few counts for accurate timing or spectral analysis. Using the number of source counts found for each source and the *Chandra* PIMMS version 4.2, we estimated unabsorbed X-ray luminosities (0.5–10 keV) using a photon index of 1.4 (Table 1). There exists marginal evidence for a sixth faint source located between C and D; however, it was not identified by either *wavdetect* or *PWDetect* (possibly due to its proximity to C and D). It would be difficult for more than one or two X-ray sources over 10 counts (translating to  $L_X(0.5\text{--}2.5\text{ keV}) > 10^{31}$  ergs/s) to be missed, apart from near source A or within  $2''$  of source D.

### 3.7. Radial Distribution

We have analyzed the radial distribution of the cluster sources by fitting generalized King model profiles using maximum likelihood techniques (see, e.g. Grindlay et al. (2002); Heinke et al. (2006); Cohn et al. (2010)). In this approach, the projected radial distribution is given by the expression,

$$S(r) = S_0 \left[ 1 + \left( \frac{r}{r_0} \right)^2 \right]^{\alpha/2}, \quad (1)$$

where  $\alpha$  is the large- $r$  power-law slope and  $r_0$  is a radial scale factor that is related to the core radius by  $r_c = (2^{-2/\alpha} - 1)^{1/2} r_0$ . We assume that the turnoff mass stellar distribution, which dominates the optical surface brightness profile, is described by a King model, i.e. by Eqn. 1 with  $\alpha = -2$  and  $r_c = r_0$ . In thermal equilibrium, the distribution of the *Chandra* sources is expected to be described by Eqn. 1 with  $\alpha_X = -3q + 1$ , where  $q = M_X/M_*$  is the ratio of the characteristic source mass to the mass of the stars that dominate the optical surface brightness profile. We here adopted the values of  $r_c = 5.8''$  and  $r_h = 29''$  from McLaughlin & van der Marel (2005) for

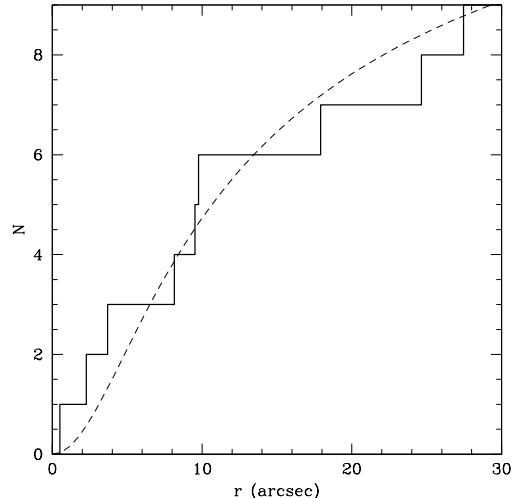


FIG. 10.— Cumulative radial distribution of *Chandra* sources in NGC 6652 (solid line) with a generalized King model fit (dashed line). The sample includes the nine sources within the half-mass radius.

the optical surface brightness profile. It is first necessary to correct the source distribution for background contamination. Based on the Giacconi et al. (2001) extragalactic source counts, we estimate a total of 2.1 background sources within the  $1' \times 8'$  subarray. We note that there is one source (L) that lies well outside of the half-mass radius, which is roughly consistent with this predicted level. This background level implies approximately 0.2 background sources within  $r_h$ . This in turn suggests that essentially all of the detected sources within  $r_h$  belong to the cluster. We note that we have not made a correction for any incompleteness due to fainter sources being lost in the vicinity of the very bright source A.

Given the small source sample, we have carried out one-parameter fits by finding the value of  $q$  which maximizes the likelihood. As in our previous work, we use bootstrap resampling to estimate the best fit parameter uncertainties. The parameters  $r_{c,X}$  and  $\alpha_X$  are expressed as functions of  $q$ , and  $S_0$  is determined by normalization. The resulting maximum likelihood value of the mass ratio is  $q = 1.17 \pm 0.28$ . The corresponding core radius and slope values are  $r_{c,X} = 5.0 \pm 0.8$  and  $\alpha_{c,X} = -2.5 \pm 1.0$ . This fit to the cumulative radial source distribution is shown in Fig. 10. For an assumed main-sequence turnoff mass (MSTO) of  $0.80 \pm 0.05 M_\odot$ , the corresponding characteristic mass for the *Chandra* sources is  $0.94 \pm 0.23 M_\odot$ . While this provides a hint that  $M_X$  exceeds the MSTO mass, the difference is clearly not statistically significant. The large statistical uncertainty is likely due to the small sample size.

We note that Noyola & Gebhardt (2006) have classified NGC 6652 as core collapsed, with an optical core radius of  $1.2''$ . As we did in our previous analysis of the *Chandra* source distribution in M30 (Lugger et al. 2007), we have fitted the radial distribution of sources with a pure power law for comparison with the optical surface brightness profile. The resulting slope is  $\alpha_X = -1.30 \pm 0.22$ . This is significantly steeper than the slope of  $-0.57 \pm 0.12$  measured by Noyola & Gebhardt (2006) for the optical cusp. In principle, comparison of these slopes can be used to estimate  $M_X$ . However, the

slope of the profile presented in their paper continuously steepens with increasing radius beyond the core, rather than maintaining a constant value for a significant run of radius as in other core collapsed clusters. The characteristic slope at  $10''$  is about  $-1.3$ , which is the same as the slope for the *Chandra* sources. This suggests a  $q$  value of unity, putting  $M_X$  near the MSTO mass. Once again, there is considerable statistical uncertainty in this value. In sum, the spatial distribution of sources does not provide a definitive estimate of the source mass.

#### 4. DISCUSSION

##### 4.1. Source A

Source A's unabsorbed X-ray luminosity is  $L_X$  (0.5–10 keV) =  $7.0_{-0.7}^{+0.7} \times 10^{35}$  ergs/s. This is comparable to our 2008 observation which found Source A to have a luminosity of  $L_X$  (0.5–6.0 keV) =  $4.4_{-0.5}^{+0.6} \times 10^{35}$  ergs/s (Coomber et al. 2011 ; our 0.5–6.0 keV luminosity is  $5.4_{-0.4}^{+0.0} \times 10^{35}$  ergs/s). Observations of XB 1832–330 previous to our 2008 observation (Sidoli et al. 2008; Tarana et al. 2007; Parmar et al. 2001) have reported X-ray luminosities several times higher. We note that the RXTE bulge scan monitoring observations (Swank & Markwardt 2001)<sup>12</sup> show a roughly sixfold drop in flux in early 2011. Our observation suggests that this decline in A's luminosity has not continued smoothly.

The scheme for dividing LMXBs into ultracompact (white dwarf donors) vs. long-period systems based on X-ray spectra (Sidoli et al. 2001) suggested Source A (XB 1832-330) as ultracompact (Parmar et al. 2001), which is ruled out by the 2.15 hour period measurement of Engel et al. (2012). This scheme may still be useful, but in dividing short-period ( $\lesssim 2$  hours) from long-period ( $\gtrsim 6$  hours) systems.

##### 4.2. Source B

The peak luminosity of Source B suggests that the system contains a neutron star; however, Source B's extreme variability is unusual for a LMXB. In May 2011, a 6.5 hour observation of NGC 6652 taken with Gemini's GMOS-S CCD detector using  $g'$  and  $r'$  filters found a similar, highly variable lightcurve for Source B (Engel et al. 2012). No clear periodicity was found.

One previously suggested explanation for Source B's behavior is a system with a high inclination angle, so that our view of the central X-ray object is obscured by the accretion disk. If this were the case, we would expect Source B's spectrum to be hardened during periods of low count rate. We see marginal evidence for this as the hardness ratio ranges from  $0.16 \pm 0.02$  for the second-lowest count rate range to  $0.23 \pm 0.02$  for the second-highest count rate range. While the tendency is not clear, the  $N_H$  does appear to decrease with increasing count rate. However, the maximum  $N_H$  ( $2.7_{-1.4}^{+1.5} \times 10^{21}$  cm $^{-2}$ ) is not sufficient to significantly decrease the count rate. An edge-on accretion disk, where flux variations are largely due to obscuration by changing  $N_H$  columns, can therefore be ruled out.

The behavior of Source B may be better explained by an instability involving the propeller effect, when the

magnetosphere of the neutron star rotates faster than the innermost region of the accretion disk, pushing material away (Illarionov & Sunyaev 1975). The location of the inner edge of the accretion disk will be determined by the ratio of gas to magnetic pressure; as gas accumulates in the disk, the disk will come closer, enabling accretion. This can produce cyclic mass transfer on a range of timescales, which have been explored in simulations by several theorists (Spruit & Taam 1993; D'Angelo & Spruit 2010; Romanova et al. 2011). Such an instability has been suggested to explain  $\sim 1$  Hz modulation in the transient LMXB SAX J1808.4–3658 (Patruno et al. 2009), and the behavior of the 'Rapid Burster' (Spruit & Taam 1993). A similar phenomenon may be responsible for the rapid flaring in Source B.

Source B has the properties of a very faint X-ray transient (VFXT). These systems typically have neutron star or black hole primaries and have peak X-ray luminosities  $10^{34} < L_X < 10^{36}$  with quiescent  $L_X$  generally an order of magnitude lower (Wijnands et al. 2006; Munro et al. 2005). Their time-averaged mass transfer rates are rather lower than expected for most evolutionary states. One explanation is that the majority of the inflowing gas is ejected, through e.g. a propeller effect. Weak and strong propeller regimes, corresponding to weak and strong outflows, have been studied by MHD simulations (Romanova et al. 2005; Ustyugova et al. 2006). If the propeller effect is truly responsible for the characteristics of Source B, it may prove important to understanding the nature of other VFXTs.

##### 4.3. Source C

The soft spectral component in Source C's spectrum is consistent with some magnetic CV spectra. Source C fits well to a simplified polar CV model, where a higher energy *mekal* component describes hard X-ray emission originating the accretion shock column front, while a lower energy blackbody component describes soft X-ray emission from the white dwarf's polar caps (Ramsay et al. 2004). While Source C is several times more luminous than the suggested polar CV X10 in 47 Tuc (Heinke et al. 2005), its spectrum is comparable. Source C may therefore be the second polar CV identified in a globular cluster.

##### 4.4. Source D

Source D's spectrum was fit well to a neutron star atmosphere model, while a *mekal* model proved to be an exceptionally poor fit. We found Source D to have low variability over our observation, while its inferred luminosity is comparable to that seen in the 2008 observation. Source D's luminosity is similar to other known quiescent LMXBs in globular clusters (Heinke et al. 2003b). As well, it lies close to the theoretical cooling track for a neutron star atmosphere on the color-magnitude diagram. We therefore suggest that Source D is a NS qLMXB.

##### 4.5. Fainter Sources

The brightest of the fainter sources, Source E's spectrum and luminosity suggest that it may be a CV. However, due to the low number of counts, the evidence is not conclusive. We were unable to adequately model Source F with any single component model, though a

<sup>12</sup> <http://asd.gsfc.nasa.gov/Craig.Markwardt//galscan/main.html>

neutron star atmosphere model proved an exceptionally poor fit. Sources H through K cannot be conclusively classified. However, most X-ray sources in globular clusters with similar luminosities and X-ray colors are CVs (Pooley & Hut 2006), with smaller fractions of chromospherically active binaries and millisecond pulsars (MSPs); therefore we may suggest the majority of our fainter sources are CVs. Due to the hardness of Source L's spectrum and its distance from the core's half-mass radius, Source L is likely a background source. This is roughly consistent with the 2.1 background sources expected from Giacconi et al. (2001) extragalactic source counts (see Section 3.7).

In 2010, NGC 6652 was detected by the *Fermi* Large Area Telescope, suggesting that the cluster hosts a substantial population of MSPs. Abdo et al. (2010) have estimated the number of MSPs in NGC 6652 to be  $54^{+27}_{-25}$ ; however, previous studies using radio observations have placed this number much lower (Kulkarni et al. 1990). A MSP coincident with NGC 6652 has recently been reported; however, it remains unclear whether it is truly associated with the cluster (DeCesar et al. 2011). MSPs could be one or more of the X-ray sources in NGC 6652. Previous observations of MSPs in other globular clusters (e.g. Bogdanov et al. (2005, 2010)) have shown that the brightest MSPs have hard spectra with luminosities typically  $<10^{32}$  erg s $^{-1}$ . Thus, some of the fainter sources in the cluster may be MSPs.

#### 4.6. X-ray Source Population

NGC 6652 is unusual in hosting two relatively bright X-ray sources. Calculations of the encounter rate,  $\Gamma$ , for NGC 6652 vary significantly, ranging from 0.2% to 2.3% of the Galactic value, depending on whether values are taken from Harris (1996) or Noyola & Gebhardt (2006). A full analysis of the effects of uncertainties in input parameters on the encounter rate is underway (Bahramian et al., in preparation). A preliminary estimate of the uncertainty in NGC 6652's encounter rate, using quoted measurements and uncertainty in surface brightness and core radius from Noyola & Gebhardt (2006), and extinction and distance measurements from Harris (2010), yields an encounter rate  $\Gamma = 1.5\text{--}4\%$  of the total Galactic globular cluster interaction rate. Such a high encounter rate would explain NGC 6652's containing two XRBs above  $10^{33}$  ergs/s.

We present cluster parameters and X-ray source numbers in three luminosity bins for several clusters in Table 4, ordered by central luminosity density. The ratio of the number of brighter to fainter X-ray sources (e.g.  $>10^{33}$  to  $10^{32\text{--}33}$  erg s $^{-1}$ , or  $10^{32\text{--}33}$  to  $10^{31\text{--}32}$  erg s $^{-1}$ ) in NGC 6652, and other clusters with very dense cores, is relatively high, indicating a relatively flat luminosity function. These data support the argument by Pooley et al. (2002b) that clusters with higher central densities have flatter luminosity functions, and the argument by Heinke et al. (2003b) that the differences above  $10^{31}$  ergs/s are driven primarily by changes within the CV population. Where detailed optical followup has been done (e.g. Pooley et al. 2002a; Edmonds et al. 2003a; Lugger et al. 2007; Cohn et al. 2010), a majority of the X-ray sources that we consider ( $L_X(0.5\text{--}2.5$  keV) $>$

$10^{31}$  ergs/s) are associated with CVs and qLMXBs.<sup>13</sup> CVs make up the majority of the two lower bins, while the top bin is comprised of accreting NSs (qLMXBs and LMXBs). So the CVs tend to show higher luminosities on average in the densest clusters; the lack of numerous qLMXBs in NGC 6652 and M15 suggests that NSs are also affected. Overall, the data suggest that clusters that reach very high central density efficiently convert their numerous lower luminosity X-ray binaries into a smaller group of higher luminosity CVs and LMXBs.

Core collapse may involve recurrent episodes of extremely high central density (Fregeau et al. 2003), in which new binaries are formed and older binaries are destroyed or ejected through interactions. The highest-density clusters are also those clusters where mass-transferring binaries are most rapidly destroyed (or ejected) through further interactions (Verbunt 2003). Binaries formed through interactions will tend to consist of two relatively massive stars. These will produce relatively high mass transfer rates, and thus relatively high  $L_X$  systems. Among CVs, magnetic channeling of accretion is required to enable high  $L_X$  (e.g. Edmonds et al. 2003b); for qLMXBs, the quiescent  $L_X$  may reflect the time-averaged mass-transfer rate (Brown et al. 1998).<sup>14</sup> As systems age, the companion is whittled away, leading to lower mass-transfer rates and thus fainter systems. In the densest systems like NGC 6652, X-ray binaries may be destroyed or ejected before they can dim significantly. The extended radial distribution of X-ray binaries in NGC 6652, particularly the large offsets of sources A and B, indeed suggests recent ejection.

#### 4.7. Future Directions

Source B's rapid X-ray and optical (Engel et al. 2012) flaring would be worth studying simultaneously (e.g. with ULTRACAM and *Chandra*), to clearly distinguish the details of accretion. Further *HST* analysis is needed to confirm (e.g. through star counts) the sharp central cusp and core-collapsed state of NGC 6652 identified through surface brightness studies by Noyola & Gebhardt (2006), as well as to identify optical counterparts of the fainter X-ray sources. If source A drops into quiescence during the *Chandra* era, a deeper study of NGC 6652's X-ray sources could confirm the unusual radial distribution and luminosity function trends we have suggested here. Detailed studies of the X-ray binary populations of other clusters of high central density, together with continuing Monte Carlo and N-body simulations, may help us to understand how core collapse proceeds.

WSS, COH & AB acknowledge support by NSERC and by an Alberta Ingenuity New Faculty Award. PWdetect has been developed by scientists at Osservatorio Astronomico di Palermo G. S. Vaiana thanks to Italian CNAA and MURST (COFIN) grants.

<sup>13</sup> This agrees with Pooley & Hut (2006) who used the 0.5–6 keV band.

<sup>14</sup> Though neutrino losses from e.g. direct URCA can reduce their quiescent  $L_X$ , Yakovlev & Pethick 2004.



TABLE 1  
 X-ray Sources in NGC 6652

Source	R.A.	Decl.	Err	Counts (0.3–7 keV)	Luminosity (0.5–10 keV)
A	18:35:43.671	-32:59:26.31	0.29	$1267^{+37}_{-36}$ $\alpha$	$7.0^{+0.7}_{-0.7} \times 10^{35}$
B	18:35:44.564	-32:59:38.49	0.28	$4634^{+69}_{-68}$	-
C	18:35:45.752	-32:59:23.24	0.30	$596^{+25}_{-24}$	-
D	18:35:45.651	-32:59:26.17	0.30	$631^{+26}_{-25}$	-
E	18:35:46.240	-32:59:29.36	0.33	$99^{+11}_{-10}$	-
F	18:35:47.743	-32:59:19.76	0.36	$35^{+7}_{-6}$	-
H	18:35:45.473	-32:59:25.48	0.40	$16^{+5}_{-4}$	$4.5^{+1.4}_{-1.1} \times 10^{31}$
I	18:35:45.818	-32:59:35.82	0.40	$15^{+5}_{-4}$	$4.2^{+1.4}_{-1.1} \times 10^{31}$
J	18:35:45.178	-32:59:34.54	0.43	$11^{+4}_{-3}$	$3.1^{+1.1}_{-0.8} \times 10^{31}$
K	18:35:44.078	-32:59:00.54	0.45	$9^{+4}_{-3}$	$2.5^{+1.1}_{-0.8} \times 10^{31}$
L	18:35:43.891	-33:00:45.63	0.72	$4^{+3}_{-2}$	$1.1^{+0.8}_{-0.6} \times 10^{31}$

NOTE. — Positions, relative position errors and counts obtained for each observed source in NGC 6652. Values for sources A-F were determined by running the CIAO tool *wavdetect* over 0.3–7 keV. Values for sources H-L were determined by running the *PWDetect* script over the same energy range. Positional errors are 95% confidence errors from Equation (5) of Hong et al. (2005). Values for errors in the counts are indicative of  $1\sigma$  and are derived from Gehrels (1986). Luminosities for sources B-F can be found in Table 3. Luminosities for sources H-L are based upon the number of counts (see text) and are listed in  $\text{erg s}^{-1}$ .  $\alpha$  From readout streak.

 TABLE 2  
 Count rates for Source B

Count Rate	Counts		Hardness	$N_H$ ( $10^{20} \text{ cm}^{-2}$ )	$kT$ keV	$L_X$ (0.5–10 keV)	$\chi^2_\nu/\text{dof}$
	0.3–1 keV	0.3–7 keV					
< 0.05	71	424	$0.17 \pm 0.02$	$23^{+11}_{-9}$	>33	$5.8^{+0.7}_{-0.7} \times 10^{33}$	1.05/10
0.05 - 0.075	67	410	$0.16 \pm 0.02$	$27^{+17}_{-15}$	>5	$1.0^{+0.2}_{-0.2} \times 10^{34}$	0.89/9
0.075 - 0.1	109	679	$0.16 \pm 0.02$	$21^{+9}_{-8}$	$16^{+36}_{-7}$	$1.4^{+0.2}_{-0.1} \times 10^{34}$	0.80/18
0.1 - 0.15	135	694	$0.20 \pm 0.02$	$13^{+8}_{-7}$	$12^{+24}_{-5}$	$1.9^{+0.2}_{-0.2} \times 10^{34}$	0.53/18
0.15 - 0.2	147	720	$0.20 \pm 0.02$	$12^{+7}_{-6}$	$7^{+8}_{-3}$	$2.4^{+0.3}_{-0.2} \times 10^{34}$	0.48/19
0.2 - 0.27	107	507	$0.21 \pm 0.02$	$10^{+8}_{-8}$	>7	$3.8^{+0.7}_{-0.5} \times 10^{34}$	0.84/12
0.27 - 0.35	130	570	$0.23 \pm 0.02$	<9	>9	$4.7^{+0.8}_{-0.8} \times 10^{34}$	1.35/14
> 0.35	106	491	$0.22 \pm 0.02$	<13	$13^{+51}_{-7}$	$6.5^{+1.1}_{-1.0} \times 10^{34}$	0.36/12

NOTE. — Number of counts observed over indicated energy ranges corresponding to particular count rate ranges. Count rate ranges are listed in counts/s. The hardness ratio is quantified by examining the fraction of counts in the low energy range (0.3–1 keV) against a larger energy range (0.3–7 keV). Errors in the hardness ratio are indicative of  $1\sigma$  and are derived from Gehrels (1986). The hydrogen column density ( $N_H$ ), plasma temperature ( $kT$ ) and luminosity are taken from fitting the spectra over each range to an absorbed hot X-ray plasma emission model (XSPEC model *phabs \* mekal*). Luminosity is in  $\text{erg s}^{-1}$ . The five ranges with the highest count rate include a pileup component.

TABLE 3  
Spectral Fits

Source	Model	$N_H$ ( $10^{20}$ cm $^{-2}$ )	$\Gamma$	kT (keV)	$L_X$ (0.5–10 keV)	$\chi^2_\nu/\text{dof}$
<b>B</b>	<b>POW</b>	$11^{+3}_{-3}$	$1.3^{+0.1}_{-0.1}$	-	$1.7^{+0.1}_{-0.1} \times 10^{34}$	1.20/39
<b>B</b>	<b>MEKAL</b>	$10^{+2}_{-2}$	-	$34^{+28}_{-13}$	$1.6^{+0.1}_{-0.1} \times 10^{34}$	1.13/39
<b>C</b>	<b>POW</b>	(5)	1.6	-	$1.3 \times 10^{33}$	4.18/14
<b>C</b>	<b>MEKAL+MEKAL</b>	<32	-	>17	$1.4^{+0.2}_{-0.2} \times 10^{33}$	1.06/11
-	<b>2<sup>nd</sup> MEKAL</b>	-	-	$0.18^{+0.03}_{-0.03}$	$3.2^{+0.8}_{-1.9} \times 10^{32}$	-
<b>C</b>	<b>MEKAL+BBODY</b>	<19	-	>18	$1.4^{+0.2}_{-0.2} \times 10^{33}$	1.05/11
-	<b>BBODY</b>	-	-	$0.07^{+0.01}_{-0.02}$	$2.3^{+6.6}_{-1.0} \times 10^{32}$	-
<b>D</b>	<b>POW</b>	$42^{+14}_{-19}$	$5.1^{+0.8}_{-1.2}$	-	$4.1^{+6.1}_{-2.1} \times 10^{33}$	0.77/14
<b>D</b>	<b>MEKAL</b>	(5)	-	1.3	$8.3 \times 10^{32}$	3.52/15
<b>D</b>	<b>NSATMOS</b>	$9^{+2}_{-2}$	-	$0.115^{+0.002}_{-0.002}$	$9.0^{+4.0}_{-2.1} \times 10^{32}$	0.65/15
<b>E</b>	<b>POW</b>	$53^{+48}_{-36}$	$2.2^{+1.1}_{-0.8}$	-	$3.8^{+3.8}_{-1.1} \times 10^{32}$	0.62/6
<b>E</b>	<b>MEKAL</b>	$34^{+35}_{-25}$	-	>1.8	$2.9^{+0.9}_{-0.7} \times 10^{32}$	0.78/6
<b>F</b>	<b>POW</b>	<35	$1.7^{+1.1}_{-0.5}$	-	$1.1^{+0.8}_{-0.5} \times 10^{32}$	1.03/1
<b>F</b>	<b>MEKAL</b>	<82	-	>1.9	$1.4^{+0.6}_{-0.5} \times 10^{32}$	1.11/1
<b>F</b>	<b>NSATMOS</b>	(5)	-	$8.5 \times 10^{-2}$	$1.3 \times 10^{32}$	6.54/2

NOTE. — Spectral fits for X-ray sources in NGC 6652. Sources B through E are fit from 0.5–10 keV; however, due to a low number of counts (42) Source F is fit from 0–10 keV. All models included absorption (XSPEC model *phabs*). For poorly fit models ( $\chi^2_\nu > 2$ )  $N_H$  was kept at the cluster value and errors were not calculated. The luminosity stated is for the unabsorbed X-ray luminosity in erg s $^{-1}$ . Two component models are continued on a second line and give the X-ray luminosity separated by components. The total unabsorbed 0.5–10 keV luminosities for Source C from the **MEKAL+MEKAL** model and the **MEKAL+BBODY** model are respectively  $1.8^{+0.1}_{-0.2} \times 10^{33}$  erg s $^{-1}$  and  $1.6^{+0.7}_{-0.2} \times 10^{33}$  erg s $^{-1}$ . The final column lists the reduced chi-squared and the degrees of freedom for each model.

TABLE 4  
Parameters and X-ray Sources of Selected Clusters

Cluster	Distance (kpc)	$\rho_0$ ( $L_{\odot} \text{ pc}^{-3}$ )	$r_c$ (pc)	$\Gamma$ (% Gal.)	Number of X-ray Sources			References
					(> $10^{33}$ )	( $10^{32-33}$ )	( $10^{31-32}$ )	
<b>47 Tuc</b>	4.5	$7.8 \times 10^4$	0.46	2.9	1	3	27	1
<b>M28</b>	5.5	$1.3 \times 10^5$	0.26	2.0	1	2	14	2,3
<b>M80</b>	10.0	$1.4 \times 10^5$	0.22	1.6	0	4	12	4
<b>NGC 6440</b>	8.5	$1.7 \times 10^5$	0.35	3.6	1	10	>13	5,3
<b>NGC 6388</b>	9.9	$2.3 \times 10^5$	0.21	3.1	0	13	27	6
<b>NGC 6752</b>	4.0	$2.3 \times 10^5$	0.13	1.2	0	1	8	7
<b>M30</b>	8.1	$3.6 \times 10^5$	0.063	0.6	1	0	3	8
<b>NGC 6397</b>	2.3	$4.1 \times 10^5$	0.041	0.3	0	2	7	9
<b>NGC 6652</b>	10.0	$1.0 \times 10^6$	0.058	2.3	2	3	4	10
<b>M15</b>	10.4	$3.5 \times 10^6$	0.050	6.7	3	2	>2	11,12

NOTE. — Parameters and X-ray source numbers from clusters with numerous published X-ray sources above  $L_X = 10^{31}$  ergs/s (Terzan 5 omitted due to uncertainty in parameters). The numbers of X-ray sources include only sources within the cluster half-mass radius, using luminosities in the 0.5–2.5 keV range from the deepest observation (or average published luminosities for M15 sources). M15 and NGC 6440 are incomplete in the lowest bin. Central luminosity densities (for the core-collapsed, we average within the core radius) and core radii are calculated using values from Noyola & Gebhardt (2006) where given, while other values are from Harris (2010). Close encounter rates  $\Gamma \propto \rho_0^{1.5} r_c^2$  are given as a percentage of the total Galactic globular cluster system rate. References: (1) Heinke et al. (2005); (2) Becker et al. (2003); (3) Heinke et al. (2003b); (4) Heinke et al. (2003a); (5) Pooley et al. (2002b); (6) Maxwell et al. (2012); (7) Pooley et al. (2002a); (8) Lugger et al. (2007); (9) Grindlay et al. (2001b); (10) this work; (11) Hannikainen et al. (2005); (12) Heinke et al. (2009).

## REFERENCES

- Abdo, A. A. et al. 2010, *A&A*, 524, A75  
 Baskill, D. S., Wheatley, P. J., & Osborne, J. P. 2005, *MNRAS*, 357, 626  
 Becker, W. et al. 2003, *ApJ*, 594, 798  
 Bogdanov, S., Grindlay, J. E., & van den Berg, M. 2005, *ApJ*, 630, 1029  
 Bogdanov, S., van den Berg, M., Heinke, C. O., Cohn, H. N., Lugger, P. M., & Grindlay, J. E. 2010, *ApJ*, 709, 241  
 Brown, E. F., Bildsten, L., & Rutledge, R. E. 1998, *ApJ*, 504, L95  
 Cash, W. 1979, *ApJ*, 228, 939  
 Cohn, H. N. et al. 2010, *ApJ*, 722, 20  
 Coomber, G., Heinke, C. O., Cohn, H. N., Lugger, P. M., & Grindlay, J. E. 2011, *ApJ*, 735, 95  
 Damiani, F., Maggio, A., Micela, G., & Sciortino, S. 1997a, *ApJ*, 483, 350  
 —. 1997b, *ApJ*, 483, 370  
 D’Angelo, C. R. & Spruit, H. C. 2010, *MNRAS*, 406, 1208  
 Davis, J. E. 2001, *ApJ*, 562, 575  
 DeCesar, M. E., Ransom, S. M., & Ray, P. S. 2011, *arXiv1111.0365*  
 Del Santo, M., Sidoli, L., Mereghetti, S., Bazzano, A., Tarana, A., & Ubertini, P. 2007, *A&A*, 468, L17  
 Deutsch, E. W., Margon, B., & Anderson, S. F. 1998, *AJ*, 116, 1301  
 Edmonds, P. D., Gilliland, R. L., Heinke, C. O., & Grindlay, J. E. 2003a, *ApJ*, 596, 1177  
 —. 2003b, *ApJ*, 596, 1197  
 Edmonds, P. D., Grindlay, J. E., Cool, A., Cohn, H., Lugger, P., & Bailyn, C. 1999, *ApJ*, 516, 250  
 Engel, M. C., Heinke, C. O., Sivakoff, G. R., El-Shamouty, K. G., & Edmonds, P. D. 2012, *ApJ*, 747, 119  
 Fregeau, J. M., Gürkan, M. A., Joshi, K. J., & Rasio, F. A. 2003, *ApJ*, 593, 772  
 Gehrels, N. 1986, *ApJ*, 303, 336  
 Giacconi, R. et al. 2001, *ApJ*, 551, 624  
 Gregory, P. C. & Lored, T. J. 1992, *ApJ*, 398, 146  
 Grindlay, J. E., Camilo, F., Heinke, C. O., Edmonds, P. D., Cohn, H., & Lugger, P. 2002, *ApJ*, 581, 470  
 Grindlay, J. E., Cool, A. M., Callanan, P. J., Bailyn, C. D., Cohn, H. N., & Lugger, P. M. 1995, *ApJ*, 455, L47  
 Grindlay, J. E., Heinke, C., Edmonds, P. D., & Murray, S. S. 2001a, *Science*, 292, 2290  
 Grindlay, J. E., Heinke, C. O., Edmonds, P. D., Murray, S. S., & Cool, A. M. 2001b, *ApJ*, 563, L53  
 Hannikainen, D. C., Charles, P. A., van Zyl, L., Kong, A. K. H., Homer, L., Hakala, P., Naylor, T., & Davies, M. B. 2005, *MNRAS*, 357, 325  
 Harris, W. E. 1996, *AJ*, 112, 1487  
 —. 2010, *ArXiv e-prints*  
 Heinke, C. O., Cohn, H. N., & Lugger, P. M. 2009, *ApJ*, 692, 584  
 Heinke, C. O., Edmonds, P. D., & Grindlay, J. E. 2001, *ApJ*, 562, 363  
 Heinke, C. O. et al. 2005, *ApJ*, 625, 796  
 Heinke, C. O., Grindlay, J. E., Edmonds, P. D., Lloyd, D. A., Murray, S. S., Cohn, H. N., & Lugger, P. M. 2003a, *ApJ*, 598, 516  
 Heinke, C. O., Grindlay, J. E., Lugger, P. M., Cohn, H. N., Edmonds, P. D., Lloyd, D. A., & Cool, A. M. 2003b, *ApJ*, 598, 501  
 Heinke, C. O., Wijnands, R., Cohn, H. N., Lugger, P. M., Grindlay, J. E., Pooley, D., & Lewin, W. H. G. 2006, *ApJ*, 651, 1098  
 Hertz, P. & Grindlay, J. E. 1983, *ApJ*, 275, 105  
 Hong, J., van den Berg, M., Schlegel, E. M., Grindlay, J. E., Koenig, X., Laycock, S., & Zhao, P. 2005, *ApJ*, 635, 907  
 Illarionov, A. F. & Sunyaev, R. A. 1975, *A&A*, 39, 185  
 Ivanova, N., Heinke, C. O., Rasio, F. A., Taam, R. E., Belczynski, K., & Fregeau, J. 2006, *MNRAS*, 372, 1043  
 King, A. R. 2000, *MNRAS*, 315, L33  
 Kulkarni, S. R., Narayan, R., & Romani, R. W. 1990, *ApJ*, 356, 174  
 Lugger, P. M., Cohn, H. N., Heinke, C. O., Grindlay, J. E., & Edmonds, P. D. 2007, *ApJ*, 657, 286  
 Maxwell, T. E. et al. 2012, *ApJ*, submitted  
 McLaughlin, D. E. & van der Marel, R. P. 2005, *ApJ Supp*, 161, 304  
 Mukai, K. & Smale, A., 2000, *ApJ*, 533, 352  
 Munro, M. P. et al. 2005, *ApJ*, 633, 228  
 Noyola, E. & Gebhardt, K. 2006, *AJ*, 132, 447  
 Parmar, A. N., Oosterbroek, T., Sidoli, L., Stella, L., & Frontera, F. 2001, *A&A*, 380, 490  
 Patruno, A., Watts, A. L., Klein-Wolt, M., Wijnands, R., & van der Klis, M. 2009, *ApJ*, 707, 1296  
 Patterson, J. & Raymond, J. C. 1985, *ApJ*, 292, 535  
 Pooley, D. & Hut, P. 2006, *ApJ*, 646, L143

- Pooley, D. et al. 2002a, *ApJ*, 569, 405  
Pooley, D. et al. 2002b, *ApJ*, 573, 184  
Ramsay, G., Cropper, M., Wu, K., Mason, K. O., Córdova, F. A., & Friedhorsky, W. 2004, *MNRAS*, 350, 1373  
Romanova, M. M., Ustyugova, G. V., Koldoba, A. V., & Lovelace, R. V. E. 2002, *ApJ*, 578, 420  
—. 2005, *ApJ*, 635, L165  
—. 2011, *MNRAS*, 416, 416  
Shara, M. M., Bergeron, L. E., Gilliland, R. L., Saha, A., & Petro, L. 1996, *ApJ*, 471, 804  
Sidoli, L., Parmar, A. N., Oosterbroek, T., Stella, L., Verbunt, F., Masetti, N., & Dal Fiume, D. 2001, *A&A*, 368, 451  
Sidoli, L., La Palombara, N., Oosterbroek, T., & Parmar, A. N. 2008, *A&A*, 488, 249  
Spruit, H. C. & Taam, R. E. 1993, *ApJ*, 402, 593  
Stacey, W. S., Heinke, C. O., Elsner, R. F., Edmonds, P. D., Weisskopf, M. C., & Grindlay, J. E. 2011, *ApJ*, 732, 46  
Swank, J. & Markwardt, K. 2001, in *ASP Conf. Ser.* 251, *New Century of X-ray Astronomy*, eds. H. Inoue & H. Kunieda (San Francisco: ASP), 94  
Tarana, A., Bazzano, A., Ubertini, P., & Federici, M. 2007, in *ESA Special Publication*, Vol. 622, *ESA Special Publication*, 437+  
Ustyugova, G. V., Koldoba, A. V., Romanova, M. M., & Lovelace, R. V. E. 2006, *ApJ*, 646, 304  
Verbunt, F. 2003, in *ASP Conf. Ser.* 296: *New Horizons in Globular Cluster Astronomy*, 245, astro-ph/0210057  
Verbunt, F., Elson, R., & van Paradijs, J. 1984, *MNRAS*, 210, 899  
Wijnands, R. et al. 2006, *A&A*, 449, 1117  
Yakovlev, D. G. & Pethick, C. J. 2004, *ARAA*, 42, 169